

Oxidative Strong Metal–Support Interaction Induced by an Amorphous TiO_x Seed Layer Boosts the Electrochemical Performance and High-Temperature Durability of Pt Nanocatalysts

Jongsu Seo,[▽] SungHyun Jeon,[▽] Siwon Lee, Dae-Kwang Lim, Jun Hyuk Kim, Jeong Hwan Kim, Sejong Ahn, and WooChul Jung*



Cite This: *ACS Catal.* 2022, 12, 8593–8600



Read Online

ACCESS |



Metrics & More



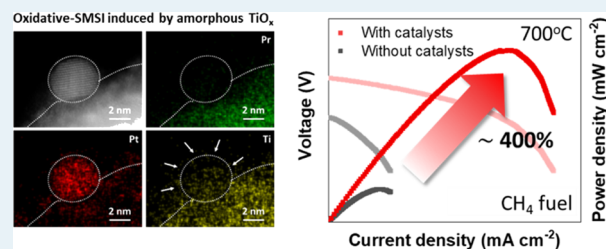
Article Recommendations



Supporting Information

ABSTRACT: Nano-sized metal particles are widely used in various chemical/electrochemical fields due to their excellent catalytic activity, but they still suffer from deactivation by sintering, and this leads to serious issues regarding the price and lifespan of catalysts. In this study, we demonstrate that the introduction of nanoscale amorphous TiO_x *via* atomic layer deposition can significantly improve the dispersion and durability of supported Pt nanocatalysts. An ultrathin TiO_x layer ($\ll 1$ nm) deposited on a conductive Pr_{0.5}Ba_{0.5}MnO₃ electrode, with a deposition time of less than 1 min, provides nucleation sites for the Pt nanocrystals impregnated thereon and promotes the migration of TiO_x to the Pt surface, creating a metal–oxide interface. As a result, when applied to ceramic fuel cells, the TiO_x undercoat achieves remarkable power density increases of over 100% and 400%, respectively, for wet (3% H₂O) H₂ and CH₄ fuels without degradation at 700 °C for 120 h. These observations provide an innovative direction for the design of supported metal catalysts for high-temperature applications.

KEYWORDS: oxidative strong metal–support interaction, atomic layer deposition, nanocatalysts, amorphous TiO_x, solid oxide fuel cell



INTRODUCTION

Solid oxide fuel cells (SOFCs) are increasingly attracting attention as a clean and efficient energy conversion device.^{1–4} SOFCs involving oxygen-ion conductive ceramic electrolytes operate at higher temperatures than other fuel cells, enabling direct utilization of hydrocarbon fuels (e.g., CH₄ and C₃H₈) in addition to pure hydrogen while also providing greater fuel selection and system design flexibility.² SOFCs therefore cannot only use hydrocarbon fuels with existing transport and storage infrastructure but also synthetic fuels based on more environmentally friendly biogas and renewable energy. However, activating hydrocarbon molecules such as CH₄ is still difficult compared to hydrogen, and irreversible degradation by carbon deposition also remains a serious technical barrier.^{2,5} In this regard, many studies have been conducted to fabricate highly active electrodes for hydrocarbon oxidation by introducing metal nanocatalysts (NCs) with excellent reactivity to CH₄ activation, but thermal/chemical stability of nanoscale metal particles at operating temperatures has still not been achieved.⁶

Meanwhile, strong metal–support interaction (SMSI) is a unique phenomenon that occurs in oxide-supported metal NCs and is currently a hot research topic in heterogeneous catalysis.^{7–10} When metal particles supported on redox-active oxides such as TiO₂, Fe₂O₃, or CeO₂ are exposed to high temperatures under a reducing atmosphere, the support oxide

atoms migrate onto metal surfaces, improving the thermal and chemical durability of the metal NCs and often enhancing the catalytic properties by forming new metal–oxide interfaces.⁷ However, despite many research efforts, this phenomenon is reversible with respect to the oxidation/reduction heat treatment cycle, and as such the effect of improving the performance of the catalyst cannot be expected in an oxygen-rich atmosphere.^{11–14} In addition, most of the reducible oxide supports (i.e., TiO₂ and CeO₂) reported to date have low electrical conductivity,^{15,16} and consequently they cannot be used as electrode materials for electrochemical devices including SOFCs.

Here, we propose for the first time that SMSI between a reducible oxide and a noble metal can be applied to a conductive complex oxide electrode *via* ALD and thus a catalyst-decorated ceramic fuel cell electrode that exhibits excellent reactivity and durability in both H₂ and CH₄ fuels is achievable. Given that SMSI-active TiO₂ or CeO₂ cannot be directly used as an electrode material due to their insufficient

Received: February 23, 2022

Revised: June 10, 2022

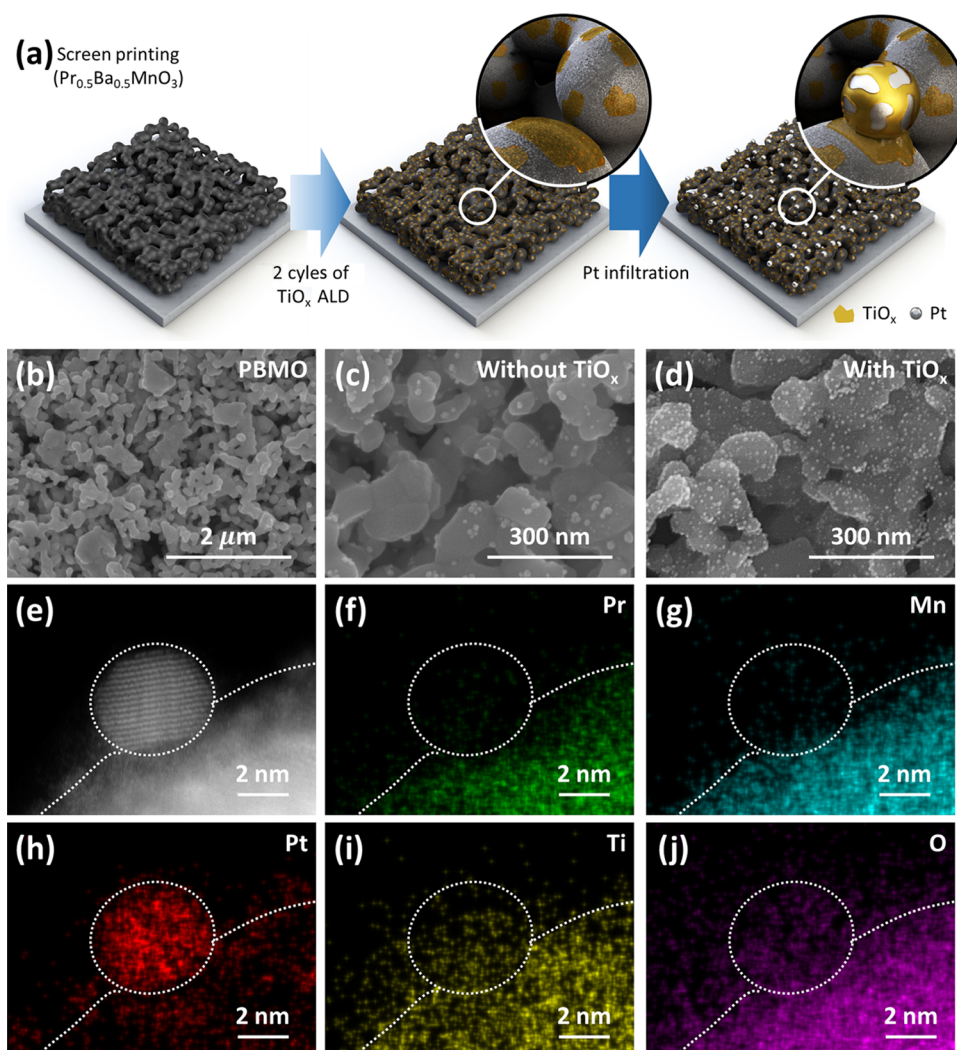


Figure 1. Microscopic images of Pt-decorated $\text{Pr}_{0.5}\text{Ba}_{0.5}\text{MnO}_3$ with and without a TiO_x seed layer. (a) Schematic flowchart of the fabrication process for the Pt NC-decorated electrode. SEM images of (b) pristine $\text{Pr}_{0.5}\text{Ba}_{0.5}\text{MnO}_3$ (PBMO) and Pt-infiltrated PBMO (c) without and (d) with the TiO_x seed layer. (e) HAADF-STEM image of magnified Pt NC and (f–j) corresponding mapping profile of Pt-infiltrated PBMO with the TiO_x seed layer (PBMO/ TiO_x /Pt).

electronic and ionic conductivity, we deposited a tiny amount ($\ll 1$ nm) of an amorphous TiO_x seed layer on conductive perovskite oxide ($\text{Pr}_{0.5}\text{Ba}_{0.5}\text{MnO}_3$ (PBMO)) and then synthesized and dispersed Pt NCs by conventional wet impregnation to create new Pt/ TiO_x interfaces. As a result, the deposited amorphous TiO_x promoted the nucleation of Pt crystals, thereby improving the particle dispersibility. More importantly, during wet impregnation, which involves an air heat treatment process, the TiO_x spontaneously migrated and partially covered the Pt surface, which protected the Pt particles from agglomeration or coking in the high-temperature CH_4 atmosphere and even under an oxidative condition. Furthermore, button cells with the Pt/ TiO_x -containing PBMO electrode show 100% and 400% augmentations of power density at 700 °C in wet H_2 and CH_4 atmospheres, respectively, as compared to the power density of the reference cell, without degradation for over 120 h. The recorded electrode performance improvement showcases that our coating method can be utilized for high-temperature electrochemical applications. In particular, unlike previous reports, the SMSI phenomenon, which is realized through oxygen heat treatment and maintained stably even in both oxidizing and

reducing atmospheres (*i.e.*, overcoming the reversibility of SMSI), suggests a new direction for future application of related catalysts.

EXPERIMENTAL METHODS

Cell Fabrication. The calcined PBMO powder as an anode and $\text{PrBa}_{0.5}\text{Sr}_{0.5}\text{Co}_{1.5}\text{Fe}_{0.5}\text{O}_3$ (PBSCF) powder as a cathode were mixed with an ink vehicle (SOFC materials) by ball-milling to form a slurry. For symmetrical half-cell preparation, PBMO ink was screen-printed onto both sides of the YSZ substrate (1 cm \times 1 cm and 0.5 mm thick) with a $\text{Ce}_{0.8}\text{Ga}_{0.2}\text{O}_2$ (GDC) thin film *via* PLD as a buffer layer. The PLD system was operated with a KrF excimer laser (Coherent COMPex Pro 205) emitting at the wavelength of 248 nm using pulsed laser energy of 300 mJ with a repetition rate of 20 Hz. It was then dried and sintered at 950 °C for 1 h at a heating rate of 5 °C/min. Pt NCs were deposited by wet infiltration from the platinum acetylacetonate ($\text{Pt}(\text{acac})_2$) solution. An electrolyte-supported cell with the PBMO|GDC| $\text{La}_{0.9}\text{Sr}_{0.1}\text{Ga}_{0.8}\text{Mg}_{0.2}\text{O}_3$ (LSGM)|GDC|PBSCF configuration was devised to demonstrate the single-cell performance. An ~ 250 nm-thick LSGM was used as an electrolyte (keracell), and a GDC film was

deposited on both sides *via* PLD as a buffer layer. PBMO ink and PBSCF ink were screen-printed on each side.

Thin TiO_x Film Preparation *via* ALD. TiO_x seed layers were deposited by ALD onto the PMBO anode with tetrakis(dimethylamido)titanium (TDMAT) as a precursor and diluted water as an oxidant at a substrate temperature of 250 °C. In a typical run, a number of cells were placed on a handmade metal holder in the middle of the reactor. A typical coating cycle followed the sequence Ti precursor dose (3 s)–Ar purge (15 s)–water dose (1 s)–Ar purge (10 s).

Physical Characterization of Prepared Electrodes. The microstructures of electrodes were examined by scanning electron microscopy (SEM, Hitachi S-4800) and energy-dispersive X-ray spectroscopy (EDX, Hitachi S-4800). The structures of Pt NCs were analyzed using the aberration-corrected TEM instrument (Titan cubed G2 60-300, FEI company) equipped with an energy-dispersive X-ray spectrometer. Inductively coupled plasma mass spectroscopy (ICP-MS, Agilent ICP-MS 7700S) was conducted to investigate the amount of deposited two cycles-TiO_x layer. Surface areas were determined from Brunauer–Emmett–Teller (BET) isotherms (3Flex, Micromeritics Company).

X-ray Photoelectron Spectroscopy. The composition and transition-metal oxidation states were analyzed using an *in situ* X-ray photoelectron spectroscopy instrument (Axis-Supra, Kratos). The temperature of the samples during the measurements was maintained at 700 °C, and the vacuum level was below 10^{−8} mbar.

Electrochemical Analysis. A symmetric cell was used for the AC impedance spectroscopy (ACIS, VSP-300, BioLogic). The AC amplitude of 20 mV at a frequency range of 1 MHz to 10 mHz was used. The cells were placed inside a continuous-flow alumina tube into which wet (3% H₂O) H₂ and CH₄ were delivered *via* digital mass flow controllers. The total flow rate was kept constant at 100 sccm (standard temperature and pressure), implying a gas velocity of 19.7 cm min^{−1}. The *I*–*V* and *I*–*P* curves were collected using the BioLogic VSP-300 device at 0.03 Vs^{−1}. An in-lab-constructed fuel-cell testing station operating at 700 °C was utilized. During the single-cell test, H₂ gas was flowed into the anode side at a flow rate of 75 mL min^{−1}, while 75 mL min^{−1} of synthetic air (N₂: 79%, O₂: 21%) was fed into the cathode side. The short-term stability data is measured with a constant voltage load of 0.65 V at 700 °C.

RESULTS AND DISCUSSION

Figure 1a shows a schematic flowchart of the fabrication process for the Pt NC-decorated electrode used in this study. It consists of two main steps. The first step is to deposit a TiO_x seed layer onto the ceramic electrode. We deposited TiO_x by two cycles of ALD using TDMAT and H₂O as a precursor and oxidant, respectively, at 250 °C (Figure S1). The uniform deposition of the TiO_x layer deposited through the process regardless of the electrode depth was confirmed through EDX analysis of cross-sectional SEM (Table S1 and Figure S2). Here, the use of only two deposition cycles, which is insufficient to form a continuous thin film, and a relatively low deposition temperature lead to distribution of the amorphous and island-like TiO_x on the electrode surface (Figure S3).^{17,18} The calculated coverage based on the BET and ICP-MS analysis for the deposited two cycles of TiO_x and corresponding description is presented in Table S2, indicating around 18% coverage of the TiO_x layer. The second step is to

synthesize and disperse Pt NCs *via* conventional impregnation onto the electrode where the ALD layer has already been deposited. In this process, to decompose the Pt precursors (C₁₀H₁₄O₄Pt, Pt(acac)₂), the electrode sample impregnated with the precursors was annealed at 500 °C in an open-air condition. Herein, we refer to the pristine PBMO sample, the PBMO sample decorated with only Pt NCs, and the sample in which the amorphous TiO_x is inserted between Pt NCs and PBMO as “PBMO”, “PBMO/Pt”, and “PBMO/TiO_x/Pt”, respectively.

First, the microstructure of prepared PBMO, PBMO/Pt, and PBMO/TiO_x/Pt samples was investigated by SEM (Figure 1b–d). Figure S4 also shows the size distribution of Pt NCs with and without the TiO_x layer. Pt NCs on TiO_x (Figure 1d) show a very small size and uniform particle distribution (7.5 ± 1.7 nm), whereas the observed Pt particles in PBMO/Pt (Figure 1c) are much larger and non-uniform (19.8 ± 5.6 nm). The enhanced dispersibility of Pt NCs is attributed to the many defects on the deposited TiO_x surface acting as nucleation sites during Pt particle formation. Higher-resolution microstructures on the prepared electrode surface were also analyzed by TEM. Figure S5a shows the high-angle annular dark-field scanning transmission electron microscope (HAADF-STEM) image of PBMO/TiO_x/Pt, and Figure S5b–d is the corresponding elemental mapping of Figure S5a. It is clearly observed that both Pt and TiO_x are evenly dispersed over the entire surface of PBMO, which is in good agreement with the previous SEM results. Figure 1e presents a HAADF-STEM image of magnified Pt NCs and corresponding elemental mapping (Figure 1f–j). In contrast to other elements such as Pr (green color) or Mn (cyan color), the signals of Ti (yellow color) and O (pink color) are more clearly observed at the same position as Pt (red color), thus showing that the undercoated TiO_x has migrated onto the Pt surface. This observation is a representative reflection of the SMSI phenomenon. Here, we would like to emphasize that the prepared sample, PBMO/TiO_x/Pt, did not undergo any high-temperature reduction process.

The strong metal–support interaction observed under oxidative conditions, the so-called oxidative strong metal–support interaction (O-SMSI), is a unique phenomenon that contradicts the previous literature.^{19–22} Recently, Wang et al. succeeded in stably maintaining oxide overlayers, which migrated to the surface of metal particles, even in an oxidative atmosphere through melamine treatment.¹⁹ They argued that melamine treatment promoted the formation of new Pt–Ti bonds, which are distinct from the commonly observed Pt–O–Ti bonds, and that these bonds are thermodynamically stable under both reducing and oxidizing conditions.^{22–24} In addition, Wei et al. also reported the existence of strong Ru–Ti bonds on amorphous TiO_x.²⁵ They suggested that during the crystallization of amorphous TiO_x, Ru clusters are formed in the open-lattice defects of TiO_x, resulting in Ru–Ti bonds, which are not observed in crystalline TiO_x. Given these recent reports, in this study, we hypothesized that the aforementioned Pt–Ti bonds were created during the formation of Pt particles on the amorphously grown TiO_x coating layer by ALD and these bonds maintained the oxide overlayer covering the Pt surface. To unravel the existence of Pt–Ti bonding depending on the defective and amorphous nature (or crystallinity) of TiO_x, we conducted *in situ* XPS measurement using the sample where the crystallinity of TiO_x was controlled through additional heat treatment. Here, the

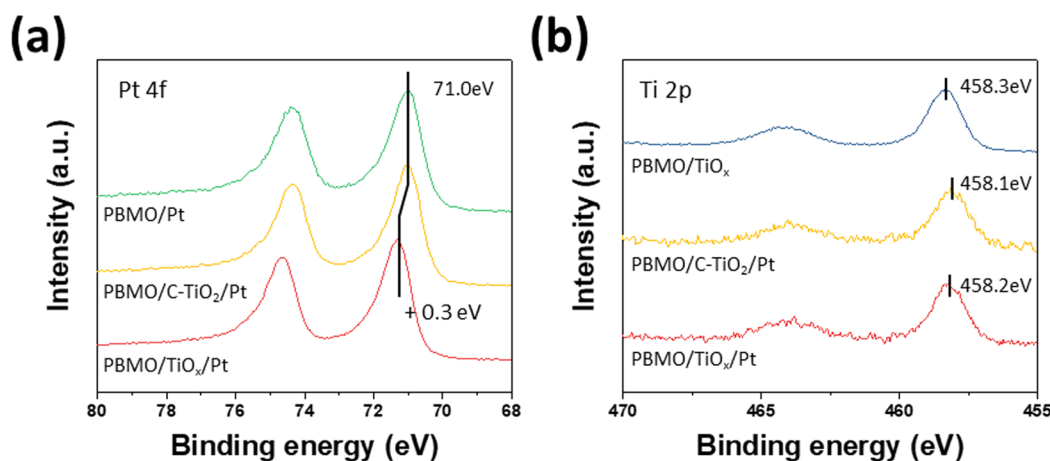


Figure 2. In situ XPS analysis. In situ XPS spectra of the (a) Pt 4f core-level spectra recorded from Pt-infiltrated $\text{Pr}_{0.5}\text{Ba}_{0.5}\text{MnO}_3$ (PBMO/Pt), Pt-infiltrated PBMO with a crystallized TiO_2 seed layer (PBMO/C- TiO_2 /Pt), and Pt-infiltrated PBMO with a TiO_x seed layer (PBMO/ TiO_x /Pt) and (b) Ti 2p core-level spectra obtained from PBMO with a TiO_x seed layer (PBMO/ TiO_x), PBMO/C- TiO_2 /Pt, and PBMO/ TiO_x /Pt at 700 °C.

comparative sample impregnated with Pt after crystallizing the deposited TiO_x is referred to as PBMO/C- TiO_2 /Pt. The amorphous TiO_x deposited on the sample surface was crystallized through annealing at 500 °C for 8 h (see the XRD results in Figure S3). *In situ* XPS measurement was taken under conditions of a temperature of 700 °C and an ultrahigh vacuum (UHV) atmosphere, and the sample was heated to 700 °C inside the analysis chamber (Figure 2). The Pt 4f core-level obtained from PBMO/Pt showed a metallic phase with the peak centered at 71.0 eV. In the case of PBMO/C- TiO_2 /Pt, the Pt 4f core-level spectrum is almost identical to that of PBMO/Pt, whereas Ti shows a lower oxidation state than that of PBMO/ TiO_x . This is consistent with the typical features of classical SMSI, in which Ti^{3+} and metallic or negatively charged Pt are observed under a reducing atmosphere.^{12,26–28}

In contrast, for the case of Pt on amorphous TiO_x , Pt 4f core-level recorded from PBMO/ TiO_x /Pt shows a positive shift of about 0.3 eV, unlike that of PBMO/C- TiO_2 /Pt. Indeed, this positive shift of Pt spectra is known as evidence that Pt–Ti bonds are formed because Pt–Ti bonds are stronger than Pt–Pt bonds.^{29–31} Therefore, we suggest that the amorphous nature of TiO_x deposited by ALD plays an important role in realizing the O-SMSI phenomenon and that strong Pt–Ti bonds are formed during the crystallization of the TiO_x undercoat.

Furthermore, we investigated the thermal stability of Pt NCs, which is considered a representative feature of SMSI, by comparing the morphology before and after annealing according to the crystallinity of TiO_x .⁷ An SEM analysis revealed that amorphous TiO_x successfully enhanced the thermal stability of Pt NCs compared with crystalline TiO_2 (Figure S6). The initial morphology of Pt NCs in PBMO/ TiO_x /Pt was successfully sustained after annealing at 650 °C under open air for 25 h (Figure S6c), whereas Pt NCs in PBMO/C- TiO_2 /Pt agglomerated after annealing (Figure S6d). The improved thermal stability is a typical feature when SMSI occurs, and this observation is thus further evidence that O-SMSI was caused by amorphous TiO_x . Indeed, we also observed dramatic enhancement of the thermal and chemical durability of Pt NCs in PBMO/ TiO_x /Pt after heat treatment at 700 °C for 25 h under wet CH_4 and H_2 , which is the typical operating condition of SOFC anodes. As presented in Figure 3, Pt NCs in PBMO/Pt show severe carbon deposition;

interestingly, however, Pt NCs in PBMO/ TiO_x /Pt retain their initial morphology without carbon deposition. In the same vein, the Fourier transform infrared (FTIR) analysis again confirms coking inhibition in PBMO/ TiO_x /Pt. Intense absorption peaks at around 1500 cm^{-1} related to graphitic sp^2 carbon owing to the formation of coked carbon^{32,33} are observed for the PBMO/Pt samples. In contrast, the PBMO/ TiO_x /Pt sample shows dramatically reduced intensity, indicating inhibited formation of graphitic carbon on Pt NCs (Figure 3c). The enhanced thermal stability results of Pt NCs with a TiO_x layer in a wet H_2 atmosphere were also presented in SEM images in Figure S7. Therefore, we find that amorphous TiO_x improves the thermal and chemical stability in both reducing and oxidizing conditions. To the best of our knowledge, this is the first study reporting thermal stability of Pt NCs supported on TiO_x and interaction with Pt particles according to TiO_x crystallinity.

Finally, we analyzed the electrochemical performance of the developed composite electrode *via* electrochemical impedance spectroscopy (EIS) in a symmetric cell configuration (PBMO|GDC|YSZ|GDC|PBMO). An ~ 100 nm GDC layer was inserted between the electrode and electrolyte to prevent undesired reaction *via* PLD. To avoid unintended catalysis for the fuel oxidation reaction, we used Au paste as a current collector. Figure S8 shows the impedance responses of the prepared electrode under a wet (3% H_2O) H_2 fuel condition at 700 °C. A typical EIS spectrum of a symmetric cell, which is plotted in the Nyquist form, commonly consists of an offset resistance at higher frequencies and a combination of semicircles at lower frequencies, the latter of which corresponds to the electrode impedance associated with the electrochemical reactions. The offset resistance is attributed to the YSZ bulk resistance and was omitted from the present spectra to reduce the degree of complexity. The dependence of the electrode resistance on the temperature is summarized in Figure 4a in an Arrhenius plot. The recorded resistance for the prepared electrodes shows a linear dependence, representing typical electrode behavior when thermally activated processes are involved. First, we found that PBMO/ TiO_x shows an almost identical resistance value and activation energy with pristine PBMO. Considering that PBMO and PBMO/ TiO_x showed similar electrode resistance, it is notable that Pt NCs were stabilized while maintaining the active sites of the

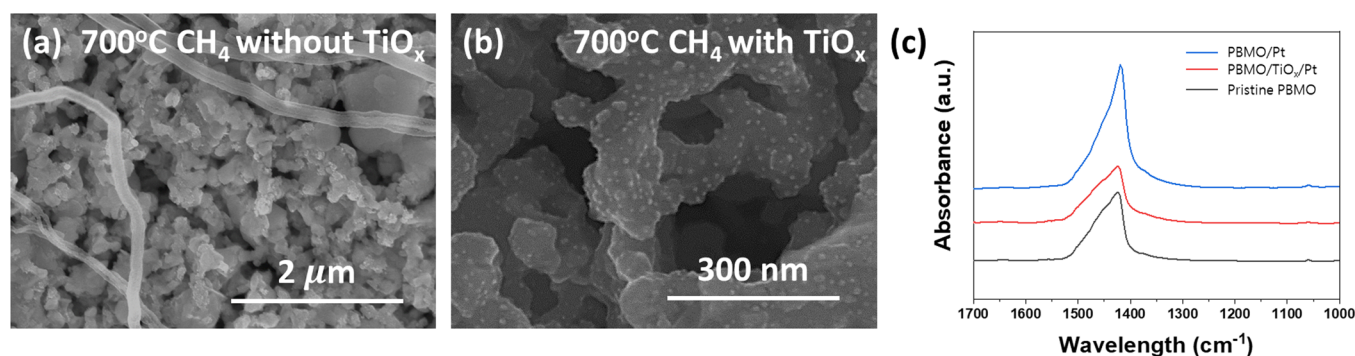


Figure 3. Thermal stability of Pt NCs with and without a TiO_x seed layer. SEM images of (a) Pt-infiltrated PBMO (PBMO/Pt) and (b) Pt-infiltrated PBMO with a TiO_x seed layer (PBMO/ TiO_x /Pt) after heat treatment at 700 °C for 25 h under a wet (3% H_2O) CH_4 atmosphere and (c) corresponding FTIR absorption spectra of the electrode after heat treatment.

electrode surface with the use of only a very small amount of TiO_x . Next, turning to the PBMO/ TiO_x /Pt electrode, we observed that its electrode resistance decreased more than five-fold compared to that of PBMO and that the activation energy for H_2 oxidation also decreased from 1.2 to 0.9 eV. Since Pt NCs are known as the best H_2 oxidation catalysts,^{32,34} it is evident that the introduction of Pt NCs improves the electrochemical performance of the PBMO electrode. Further, the electrochemical performance of electrodes for wet (3% H_2O) methane fuel was subsequently investigated at 700 °C after measuring the electrode activity under H_2 fuel. As well as using H_2 fuel, for CH_4 , the PBMO/ TiO_x /Pt electrode showed huge improvement (ASR, area-specific resistance: $1.6 \Omega \text{ cm}^2$) compared with the pristine PBMO electrode (ASR: $18.8 \Omega \text{ cm}^2$) (Figure S9). The obtained polarization resistance levels of the PBMO/ TiO_x /Pt electrode are shown in Figure 4b with those of other ceramic anodes for comparison. Open symbols indicate the electrode resistance obtained under H_2 fuel and closed symbols represents the electrode resistance using CH_4 fuel. It can be seen that the developed electrode has comparable ASR and especially robust electrode activity for CH_4 fuel with other ceramic electrodes through successful stabilization of Pt NCs without sacrificing the active sites.

Lastly, we evaluate the developed electrode using electrolyte-supported cells based on an $\sim 250 \mu\text{m}$ -thick LSGM electrolyte. The fuel cell performance of a single-cell with a configuration of PBMO|GDC|LSGM|GDC|PBSCF was tested using humidified (3% H_2O) H_2 and CH_4 and synthetic air as an oxidant. To avoid any catalytic activity for fuel oxidation, Au paste and Au mesh were applied as the current collector. As shown in Figure 4c,d, the maximum power densities of the cell containing PBMO without any catalysts in H_2 and CH_4 were about 180 and 5 mW, which are consistent with results in the literature.³⁵ In the case of the cell containing PBMO/ TiO_x /Pt, the maximum power densities were dramatically increased by more than 100% in H_2 fuel and 400% in CH_4 fuel. Furthermore, to verify the stability of the PBMO/ TiO_x /Pt electrode in real SOFC operating conditions, we measured the short-term stability with a constant voltage load of 0.65 V at 700 °C in both H_2 and CH_4 fuel (Figure S10 and Figure 4e). We observed that there is no remarkable degradation, indicating excellent stability of Pt NCs during actual SOFC operation *via* insertion of a tiny amount of TiO_x .

It should be notable that the strategy reported in this work is suitable as a practical and scalable manufacturing route for commercial SOFC electrodes. Both electrodes and catalysts

were fabricated through the most commonly used process in the SOFC field, and only an ALD process and the source for TiO_x , which is commercially available in the semiconductor industry, were added. ALD does not require high-temperature heat treatment or a UHV, and the required deposition process in this work is very fast (*e.g.*, the deposition time of two cycles of TiO_x was less than one minute). Further, since ALD is not dependent on the selection of electrode materials and operating conditions of the device, this strategy is not limited to the PBMO, TiO_x , and Pt combinations employed in this study. To identify whether this strategy is applicable to other material combinations and applications, we investigated the behavior of metal NCs on $\text{La}_{0.75}\text{Sr}_{0.25}\text{Cr}_{0.5}\text{Mn}_{0.5}\text{O}_3$ (LSCM)^{36,37} and $\text{La}_{0.6}\text{Sr}_{0.4}\text{Co}_{0.2}\text{Fe}_{0.8}\text{O}_3$ (LSCF),^{38,39} which are conventional SOFC ceramic electrodes (the detailed results are provided in Figures S11 and S12). Interestingly, for the case of LSCM, Pt NCs on LSCM with three cycles of TiO_x show high thermal stability under an air condition at 700 °C for 25 h while maintaining their initial microstructure (Figure S11). In addition, the LSCM/ TiO_x /Pt electrode showed dramatically improved performance (more than eight-fold) with excellent stability over time. As seen in Figure 2, since amorphous TiO_x facilitates the SMSI with metal NCs, it is possible to obtain a highly active electrode with excellent durability even under oxidative operating conditions. Therefore, it can be seen that the strategy proposed in this study is not limited to only PBMO, TiO_x , and Pt combinations and these results suggest the potential of utilizing this strategy not only for SOFC anodes but also in various high-temperature applications such as SOFC cathodes, proton-conducting fuel cells (PCFCs), etc.

CONCLUSIONS

In this study, we introduced an amorphous TiO_x seed layer for stabilizing Pt NCs by using strong metal–support interaction (SMSI) on SOFC anodes to achieve high and stable performance with methane as a fuel. We confirmed that ALD, a process requiring less than a minute, effectively improves the thermal/chemical stability of Pt NCs at 700 °C by uniformly depositing the TiO_x seed layer over the entire electrode surface, forming strong chemical bonds with the deposited Pt NCs. At this time, a very small amount of amorphous TiO_x seed layer was used for stabilizing the NCs through two cycles of ALD, and therefore it can stabilize Pt NCs without sacrificing the active sites of PBMO. Through the fabrication of the button cell using the developed electrode, it

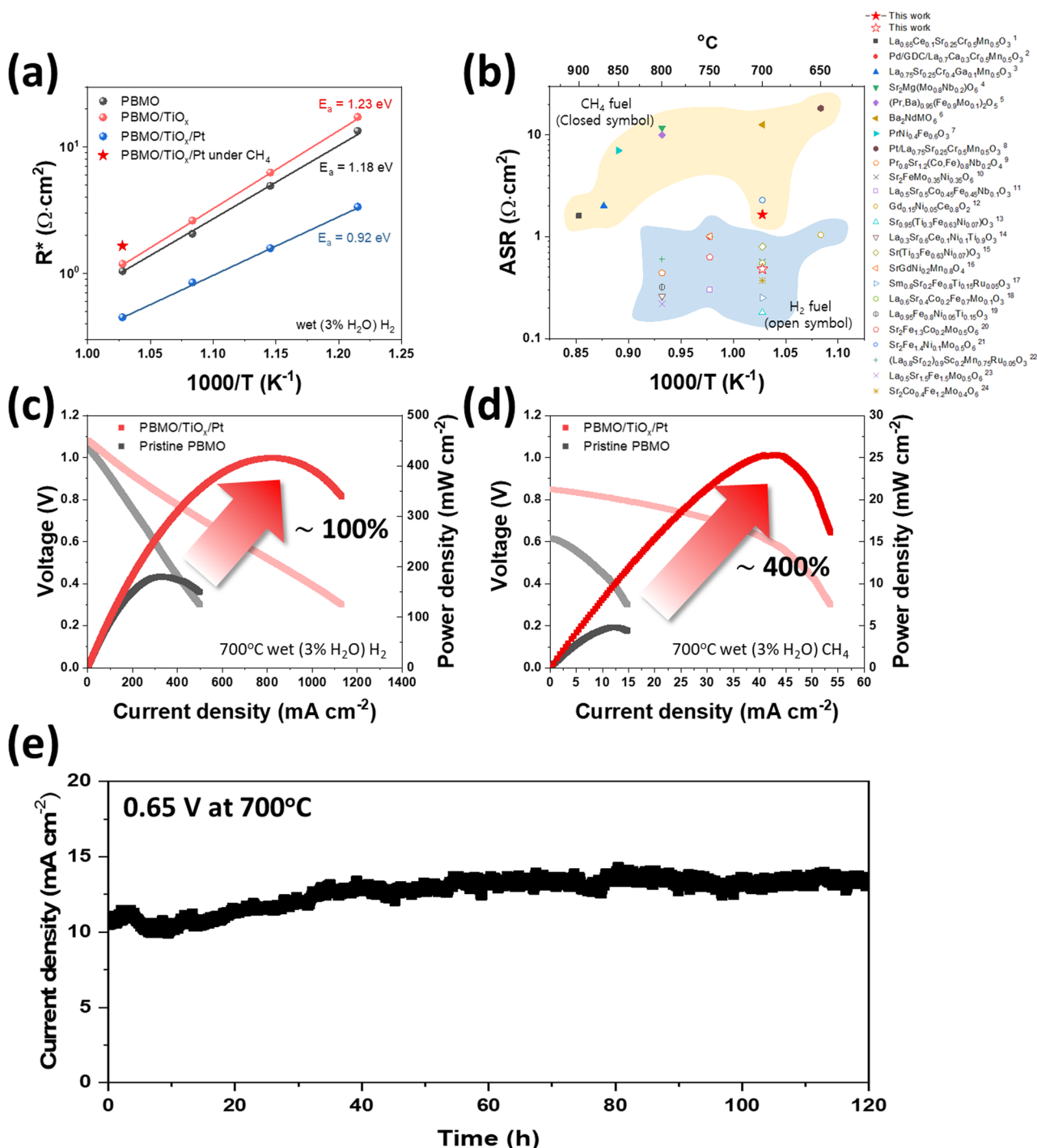


Figure 4. Electrochemical reactivity of PBMO/TiO_x/Pt under H₂ and CH₄ fuel. (a) Temperature dependence of the electrode resistance normalized by area of pristine Pr_{0.5}Ba_{0.5}MnO₃ (PBMO), PBMO with a TiO_x seed layer (PBMO/TiO_x), and Pt-infiltrated PBMO with a TiO_x seed layer (PBMO/TiO_x/Pt). The red closed star symbol in panel (a) represents the electrode resistance of PBMO/TiO_x/Pt obtained using wet (3% H₂O) CH₄ fuel. (b) Selected electrode resistance of PBMO/TiO_x/Pt (obtained at 700 °C) and the reported electrode resistances of other ceramic electrodes (references are provided in the Supporting Information). Open symbols and closed symbols represent the electrode resistance using H₂ fuel and CH₄ fuel, respectively. Current–voltage curves and the corresponding power densities of pristine PBMO and PBMO/TiO_x/Pt cell using humidified (3% H₂O) (c) H₂ and (d) CH₄. (e) Short-term stability for a PBMO/TiO_x/Pt cell under a constant voltage load of 0.65 V at 700 °C in humidified CH₄. Results reproduced in panel (b) in the manuscript have permission from refs 1–24 in the Supporting Information.

was found that the power density was improved by 100% and 400%, respectively, when using H₂ fuel and CH₄ fuel. Furthermore, we revealed that amorphous TiO_x facilitates the SMSI even under an oxidative condition and therefore the developed strategy is not limited to specific material combinations or gas atmospheres. Through this, we can

provide the possibility of expanding the developed technology to various applications. Based on these findings, we suggest a new strategy to fabricate a highly durable and active electrode by realizing unique metal NC properties while maintaining maximized active sites *via* the introduction of ALD within 1 min process.

■ ASSOCIATED CONTENT

SI Supporting Information

The Supporting Information is available free of charge at <https://pubs.acs.org/doi/10.1021/acscatal.2c00947>.

Growth rate per cycle as a function of the precursor pulse time; Confirmation result of deposition uniformity of the TiO_x layer; Corresponding cross-sectional SEM; XRD patterns of TiO_x film; Calculated surface coverage of two cycle-TiO_x; corresponding size distribution of Pt NCs; HAADF images; typical impedance spectra of the electrode; and electrochemical stability test in a H₂ atmosphere (PDF)

■ AUTHOR INFORMATION

Corresponding Author

WooChul Jung – Materials Science and Engineering, Korea Advanced Institute of Science and Technology (KAIST), Daejeon 34141, Republic of Korea; orcid.org/0000-0001-5266-3795; Email: wjung@kaist.ac.kr

Authors

Jongsu Seo – Hydrogen Research Department, Korea Institute of Energy Research (KIER), Daejeon 34129, Republic of Korea

SungHyun Jeon – Materials Science and Engineering, Korea Advanced Institute of Science and Technology (KAIST), Daejeon 34141, Republic of Korea; orcid.org/0000-0003-2472-4436

Siwon Lee – Materials Science and Engineering, Korea Advanced Institute of Science and Technology (KAIST), Daejeon 34141, Republic of Korea; Current address: Department of Chemical and Biomolecular Engineering, University of Pennsylvania, Philadelphia, Pennsylvania 19104, United States

Dae-Kwang Lim – Materials Science and Engineering, Korea Advanced Institute of Science and Technology (KAIST), Daejeon 34141, Republic of Korea; Current address: New Energy Technology Laboratory, Korea Electric Power Corp. Research Institute, Daejeon 34056, Republic of Korea

Jun Hyuk Kim – Materials Science and Engineering, Korea Advanced Institute of Science and Technology (KAIST), Daejeon 34141, Republic of Korea; Current address: Department of Chemical Engineering, Hongik University, Seoul 04066, Republic of Korea

Jeong Hwan Kim – Materials Science and Engineering, Hanbat National University, Daejeon 34158, Republic of Korea

Sejong Ahn – Materials Science and Engineering, Korea Advanced Institute of Science and Technology (KAIST), Daejeon 34141, Republic of Korea

Complete contact information is available at <https://pubs.acs.org/doi/10.1021/acscatal.2c00947>

Author Contributions

[†]J.S. and S.H.J. contributed equally.

Notes

The authors declare no competing financial interest.

■ ACKNOWLEDGMENTS

This research was supported by National R&D Program through the National Research Foundation of Korea (NRF)

funded by the Ministry of Science and ICT, grant numbers 2020M3H4A3105824 and NRF-2021R1A6A3A01087240.

■ REFERENCES

- (1) Minh, N. Q. CERAMIC FUEL-CELLS. *J. Am. Ceram. Soc.* **1993**, *76*, 563–588.
- (2) McIntosh, S.; Gorte, R. J. Direct hydrocarbon solid oxide fuel cells. *Chem. Rev.* **2004**, *104*, 4845–4866.
- (3) Seo, J.; Kim, S.; Jeon, S.; Kim, S.; Kim, J. H.; Jung, W. Nanoscale interface engineering for solid oxide fuel cells using atomic layer deposition. *Nanoscale Adv.* **2022**, *4*, 1060–1073.
- (4) Azizi, M. A.; Brouwer, J. Progress in solid oxide fuel cell-gas turbine hybrid power systems: System design and analysis, transient operation, controls and optimization. *Appl. Energy* **2018**, *215*, 237–289.
- (5) Gao, Z.; Moggi, L. V.; Miller, E. C.; Railsback, J. G.; Barnett, S. A. A perspective on low-temperature solid oxide fuel cells. *Energy Environ. Sci.* **2016**, *9*, 1602–1644.
- (6) Cao, A.; Veser, G. Exceptional high-temperature stability through distillation-like self-stabilization in bimetallic nanoparticles. *Nat. Mater.* **2010**, *9*, 75–81.
- (7) van Deelen, T. W.; Mejia, C. H.; de Jong, K. P. Control of metal-support interactions in heterogeneous catalysts to enhance activity and selectivity. *Nat. Catal.* **2019**, *2*, 955–970.
- (8) Gao, C. B.; Lyu, F. L.; Yin, Y. D. Encapsulated Metal Nanoparticles for Catalysis. *Chem. Rev.* **2021**, *121*, 834–881.
- (9) Wang, L.; Wang, L.; Meng, X.; Xiao, F.-S. New Strategies for the Preparation of Sinter-Resistant Metal-Nanoparticle-Based Catalysts. *Adv. Mater.* **2019**, *31*, 1901905.
- (10) Zhang, Z.; Liu, J.; Gu, J.; Su, L.; Cheng, L. An overview of metal oxide materials as electrocatalysts and supports for polymer electrolyte fuel cells. *Energy Environ. Sci.* **2014**, *7*, 2535–2558.
- (11) Haller, G. L.; Resasco, D. E. METAL SUPPORT INTERACTION - GROUP-VIII METALS AND REDUCIBLE OXIDES. *Adv. Catal.* **1989**, *36*, 173–235.
- (12) Fu, Q.; Wagner, T.; Olliges, S.; Carstanjen, H. D. Metal-oxide interfacial reactions: Encapsulation of Pd on TiO₂ (110). *J. Phys. Chem. B* **2005**, *109*, 944–951.
- (13) Tauster, S. J. STRONG METAL-SUPPORT INTERACTIONS. *Acc. Chem. Res.* **1987**, *20*, 389–394.
- (14) Tauster, S. J.; Fung, S. C.; Garten, R. L. STRONG METAL-SUPPORT INTERACTIONS - GROUP-8 NOBLE-METALS SUPPORTED ON TiO₂. *J. Am. Chem. Soc.* **1978**, *100*, 170–175.
- (15) Chiang, Y. M.; Lavik, E. B.; Blom, D. A. Defect thermodynamics and electrical properties of nanocrystalline oxides: Pure and doped CeO₂. *Nanostruct. Mater.* **1997**, *9*, 633–642.
- (16) Nowotny, M. K.; Bak, T.; Nowotny, J. Electrical properties and defect chemistry of TiO₂ single crystal. I. Electrical conductivity. *J. Phys. Chem. B* **2006**, *110*, 16270–16282.
- (17) Mackus, A. J. M.; Verheijen, M. A.; Leick, N.; Bol, A. A.; Kessels, W. M. M. Influence of Oxygen Exposure on the Nucleation of Platinum Atomic Layer Deposition: Consequences for Film Growth, Nanopatterning, and Nanoparticle Synthesis. *Chem. Mater.* **2013**, *25*, 1905–1911.
- (18) Lu, J.; Elam, J. W.; Stair, P. C. Synthesis and Stabilization of Supported Metal Catalysts by Atomic Layer Deposition. *Acc. Chem. Res.* **2013**, *46*, 1806–1815.
- (19) Liu, S.; Qi, H.; Zhou, J.; Xu, W.; Niu, Y.; Zhang, B.; Zhao, Y.; Liu, W.; Ao, Z.; Kuang, Z.; Li, L.; Wang, M.; Wang, J. Encapsulation of Platinum by Titania under an Oxidative Atmosphere: Contrary to Classical Strong Metal-Support Interactions. *ACS Catal.* **2021**, *11*, 6081–6090.
- (20) Tang, M.; Li, S.; Chen, S.; Ou, Y.; Hiroaki, M.; Yuan, W.; Zhu, B.; Yang, H.; Gao, Y.; Zhang, Z.; Wang, Y. Facet-Dependent Oxidative Strong Metal-Support Interactions of Palladium-TiO₂ Determined by In Situ Transmission Electron Microscopy. *Angew. Chem., Int. Ed.* **2021**, *60*, 22339–22344.
- (21) Du, X.; Tang, H.; Qiao, B. Oxidative Strong Metal-Support Interactions. *Catalysts* **2021**, *11*, 896.

- (22) Liu, S.; Xu, W.; Niu, Y.; Zhang, B.; Zheng, L.; Liu, W.; Li, L.; Wang, J. Ultrastable Au nanoparticles on titania through an encapsulation strategy under oxidative atmosphere. *Nat. Commun.* **2019**, *10*, 5790.
- (23) Matsubu, J. C.; Zhang, S.; DeRita, L.; Marinkovic, N. S.; Chen, J. G. G.; Graham, G. W.; Pan, X.; Christopher, P. Adsorbate-mediated strong metal-support interactions in oxide-supported Rh catalysts. *Nat. Chem.* **2017**, *9*, 120–127.
- (24) Li, S.; Xu, Y.; Chen, Y.; Li, W.; Lin, L.; Li, M.; Deng, Y.; Wang, X.; Ge, B.; Yang, C.; Yao, S.; Xie, J.; Li, Y.; Liu, X.; Ma, D. Tuning the Selectivity of Catalytic Carbon Dioxide Hydrogenation over Iridium/Cerium Oxide Catalysts with a Strong Metal-Support Interaction. *Angew. Chem., Int. Ed.* **2017**, *56*, 10761–10765.
- (25) Zhou, Y.; Xie, Z.; Jiang, J.; Wang, J.; Song, X.; He, Q.; Ding, W.; Wei, Z. Lattice-confined Ru clusters with high CO tolerance and activity for the hydrogen oxidation reaction. *Nat. Catal.* **2020**, *3*, 454–462.
- (26) Bahl, M. K.; Tsai, S. C.; Chung, Y. W. AUGER AND PHOTOEMISSION INVESTIGATIONS OF THE PLATINUM-SR/TIO₃(100) INTERFACE - RELAXATION AND CHEMICAL-SHIFT EFFECTS. *Phys. Rev. B* **1980**, *21*, 1344–1348.
- (27) Beck, A.; Huang, X.; Artiglia, L.; Zabilskiy, M.; Wang, X.; Rzepka, P.; Palagin, D.; Willinger, M. G.; van Bokhoven, J. A. The dynamics of overlayer formation on catalyst nanoparticles and strong metal-support interaction. *Nat. Commun.* **2020**, *11*, 3220.
- (28) Ohyama, J.; Yamamoto, A.; Teramura, K.; Shishido, T.; Tanaka, T. Modification of Metal Nanoparticles with TiO₂ and Metal-Support Interaction in Photodeposition. *ACS Catal.* **2011**, *1*, 187–192.
- (29) Beard, B. C.; Ross, P. N. CHARACTERIZATION OF A TITANIUM-PROMOTED SUPPORTED PLATINUM ELECTRO-CATALYST. *J. Electrochem. Soc.* **1986**, *133*, 1839–1845.
- (30) Kawasoe, Y.; Tanaka, S.; Kuroki, T.; Kusaba, H.; Ito, K.; Teraoka, Y.; Sasaki, K. Preparation and electrochemical activities of Pt-Ti alloy PEFC electrocatalysts. *J. Electrochem. Soc.* **2007**, *154*, B969–B975.
- (31) Sedona, F.; Rizzi, G. A.; Agnoli, S.; Xamena, F.; Papageorgiou, A.; Ostermann, D.; Sambì, M.; Finetti, P.; Schierbaum, K.; Granozzi, G. Ultrathin TiO_x films on Pt(111): A LEED, XPS, and STM investigation. *J. Phys. Chem. B* **2005**, *109*, 24411–24426.
- (32) Seo, J.; Tsvetkov, N.; Jeong, S. J.; Yoo, Y.; Ji, S.; Kim, J. H.; Kang, J. K.; Jung, W. Gas-Permeable Inorganic Shell Improves the Coking Stability and Electrochemical Reactivity of Pt toward Methane Oxidation. *ACS Appl. Mater. Interfaces* **2020**, *12*, 4405–4413.
- (33) Cai, Z. J.; Zhang, Q.; Song, X. Y. Improved electrochemical performance of polyindole/carbon nanotubes composite as electrode material for supercapacitors. *Electron. Mater. Lett.* **2016**, *12*, 830–840.
- (34) Choi, Y.; Cha, S.; Ha, H.; Lee, S.; Seo, H.; Lee, J.; Kim, H.; Kim, S.; Jung, W. Unravelling inherent electrocatalysis of mixed-conducting oxide activated by metal nanoparticle for fuel cell electrodes. *Nat. Nanotechnol.* **2019**, *14*, 245.
- (35) Sengodan, S.; Choi, S.; Jun, A.; Shin, T. H.; Ju, Y. W.; Jeong, H. Y.; Shin, J.; Irvine, J. T. S.; Kim, G. Layered oxygen-deficient double perovskite as an efficient and stable anode for direct hydrocarbon solid oxide fuel cells. *Nat. Mater.* **2015**, *14*, 205–209.
- (36) Shin, J.; Lee, Y. J.; Jan, A.; Choi, S. M.; Park, M. Y.; Choi, S.; Hwang, J. Y.; Hong, S.; Park, S. G.; Chang, H. J.; Cho, M. K.; Singh, J. P.; Chae, K. H.; Yang, S.; Ji, H. I.; Kim, H.; Son, J. W.; Lee, J. H.; Kim, B. K.; Lee, H. W.; Hong, J.; Lee, Y. J.; Yoon, K. J. Highly active and thermally stable single-atom catalysts for high-temperature electrochemical devices. *Energy Environ. Sci.* **2020**, *13*, 4903–4920.
- (37) Tao, S. W.; Irvine, J. T. S. A redox-stable efficient anode for solid-oxide fuel cells. *Nat. Mater.* **2003**, *2*, 320–323.
- (38) Chen, Y.; Choi, Y.; Yoo, S.; Ding, Y.; Yan, R.; Pei, K.; Qu, C.; Zhang, L.; Chang, I.; Zhao, B.; Zhang, Y.; Chen, H.; Chen, Y.; Yang, C.; de Glee, B.; Murphy, R.; Liu, J.; Liu, M. A Highly Efficient Multi-phase Catalyst Dramatically Enhances the Rate of Oxygen Reduction. *Joule* **2018**, *2*, 938–949.
- (39) Ni, C.; Zhou, J.; Zhang, Z.; Li, S.; Ni, J.; Wu, K.; Irvine, J. T. S. Iron-based electrode materials for solid oxide fuel cells and electrolyzers. *Energy Environ. Sci.* **2021**, *14*, 6287–6319.